Powder Technology 377 (2021) 966–973

Contents lists available at ScienceDirect

Powder Technology

journal homepage: www.elsevier.com/locate/powtec

Evolving surface properties of stirred wet milled aluminum-doped titanium dioxide: A discretely heterogeneous system

David Austin [a], Ali Hassanpour [a], Timothy N. Hunter [a], John Robb [b], John L. Edwards [b], Stephen Sutcliffe [b], Jae W. Lee [c], David Harbottle [a,*]

[a] School of Chemical and Process Engineering, University of Leeds, Leeds, UK
[b] Venator Ltd., Titanium House, Stockton-on-Tees, UK
[c] Department of Chemical and Biomolecular Engineering, Korea Advanced Institute of Science and Technology (KAIST), Daejeon, Republic of Korea

ARTICLE INFO

Article history:
Received 24 April 2020
Received in revised form 31 August 2020
Accepted 17 September 2020
Available online 22 September 2020

Keywords:
Milling
Heterogeneous particles
Iso-electric point
Surface science

ABSTRACT

The stirred wet milling of aluminum-doped TiO_2 was considered. At milling speeds of 2500–6000 rpm, the $pH_{i.e.p.}$ shifted from pH 5.7 to pH ~8, while at 8000 rpm the shift in $pH_{i.e.p.}$ was smaller. Milling at 8000 rpm, the reduced milling performance was attributed to a change in the predominant milling mechanism. XPS revealed an approximate linear correlation between the relative surface alumina content (at.%) and particle specific surface area, with the shifting $pH_{i.e.p.}$ corresponding to the surface alumina. The lower $pH_{i.e.p.}$ at 8000 rpm was rationalized by high resolution TEM image analysis. Samples milled at 8000 rpm (beyond mill energies used in pigment production) produced a significant quantity of ultra-fines ($d_{50} \ll 50$ nm) which coated the larger particles. These ultra-fines were predominately titania-like and suppressed the shift in $pH_{i.e.p.}$. The study confirmed the aluminum-doped TiO_2 particles were initially titania surface-rich with bulk alumina increasingly exposed during milling.

1. Introduction

Titanium dioxide (TiO_2) is a key industrial product in coatings, inks and plastics, used exclusively over other materials as a source of light scattering [1–3], with its enhanced properties attributed to the high refractive index [4] with values of 2.74 and 2.54 for the two polymorphs, rutile and anatase respectively [1]. The rutile polymorph provides a higher refractive index than any other stable colorless material [1], and thus has excellent scattering properties [3]. The optical performance of titanium dioxide also relates to its particle size, with a particle size of ~0.2–0.4 μm being optimal for visible light scattering [5]. Furthermore, a narrow particle size distribution is desirable, with fine and coarse particles adversely affecting opacity and gloss properties respectively [6].

TiO_2 is predominantly manufactured via the chloride process, where titanium tetrachloride ($TiCl_4$) is oxidised in a flame or oxygen plasma to form TiO_2 at temperatures >1000 °C [7]. Anatase is the kinetically formed polymorph in the flame synthesis of $TiCl_4$, reported as the dominant polymorph at elevated temperatures of 1450 °C [8]. Consequently, ≤5 mol% aluminum trichloride ($AlCl_3$) is added during oxidation to preferentially form the rutile polymorph [9].

Aluminum (from $AlCl_3$) incorporation into the TiO_2 crystal structure is debated, with Al^{3+} reported to substitute for Ti^{4+} within the lattice structure [10,11]; with the lower charge of Al^{3+} resulting in the substitutional solid solution having oxygen vacancies. These vacancies are considered to aid transformation of anatase to rutile, which involves both volume contraction and cooperative movement of titanium (Ti^{4+}) and oxygen (O^{2-}) ions [12]. This contrasts the thermodynamic consideration, where it has been shown that $AlCl_3$ doping stabilizes both phases [13], or even facilitates the transformation of rutile to anatase [14]. Contrastingly, Sleptys and Vaughan [15] concluded that Al^{3+} ions enter the crystal structure interstitially.

Discrepancy regarding the location of Al_2O_3 within the primary particle remains. Using XPS, Garbassi et al. [16] observed no surface Al for TiO_2 particles synthesized via the sulfate process, doping Al_2O_3 at 0.02 to 0.2 wt% in the temperature range of 723 K to 1238 K, with and without 3 wt% rutile particle seeds. With rutile particle seeds, the formed TiO_2 particles were a mixture of both polymorphs, with a significant increase in the rutile content from 4 to >99 wt% when the temperature was increased from 1113 K to 1238 K (as determined by X-ray diffraction, XRD). Across this polymorphic transition temperature range, acid leaching tests confirmed more surface Al, with the authors commenting that the anatase-to-rutile transformation favors the segregation of alumina. However, the authors also noted that the leaching tests recovered <50% of the dopant concentration, suggesting that Al has a '*marked preference for the bulk of the material*' [16].

* Corresponding author.
E-mail address: d.harbottle@leeds.ac.uk (D. Harbottle).

https://doi.org/10.1016/j.powtec.2020.09.033

Tsai et al. [11] synthesized Al-doped TiO_2 with dopant concentrations of 0, 0.1, 0.3 and 0.5 Al/Ti mass ratios. With compositions of anatase to rutile of 0.64, 0.63, 0.60 and 0.54, and surface atomic concentrations (at.%) of Al of 0, 6.8, 10.5 and 22.1 (for increasing Al/Ti mass ratios), the data suggested that Al was preferentially retained within the bulk. It should be noted that these samples were laboratory synthesized at significantly higher dopant concentrations and at lower temperatures (6 kW plasma torch) than industrial processes.

In contrast, Gesenhues [17] studied the calcination of TiO_2 using concentrations of Al_2O_3 up to 1% Al_2O_3/TiO_2, observing significantly more Al_2O_3 at the particle surface. Moreover, for dopant concentrations ≥0.8 wt%, the surface saturated at 8–10 μmol of Al per m^2 of specific surface area, in agreement with the calculated surface saturation, assuming all surface rutile titania cation sites (Ti^{4+}) were substituted with alumina cations (Al^{3+}) [17].

Using time-of-flight ion mass spectroscopy and XPS analysis, Taylor et al. [9] compared bulk and surface alumina content of Al-doped TiO_2 prepared by the chloride process, with dopant concentrations from 0.33 to 1.18 wt%. Increasing the dopant concentration led to greater inclusion of alumina in the bulk and at the particle surface, although the surface concentration was higher and the particle surface saturated at ~12 at.%. Johansson and Losoi [18] reported that the majority of Al_2O_3 resides at the particle surface when studying particles synthesized by both the chloride and sulfate processes, and dry-ball milled prior to analysis. The authors noted a surface concentration of Al equal to 19.4 at.%, which exceeded the empirical surface saturation discussed by Taylor et al. [9]

Taylor et al. [9] also studied the influence of Al_2O_3 doping on the dispersion properties of TiO_2, with the pH-dependent maximum yield stress and particle isoelectric point ($pH_{i.e.p.}$) increasing with more surface alumina, as well as observing broadening of the pH-dependent yield stress curve, which was attributed to the increased particle surface heterogeneity. Furthermore, both the pH-dependent maximum yield stress and $pH_{i.e.p.}$ showed a linear correlation with surface alumina content (at.%). Interestingly, dispersion behavior analogous to pure α–aluminum oxide was observed at alumina surface contents of ~9 to 10 at.%.

For pigment applications sub-micron particles (~0.2 μm) are desired, with fine grinding of coarse particle aggregates frequently achieved by stirred media mills [3], with a rotating agitator and grinding chamber operated at a media bead fill ratio of ~0.8 to 0.85 [19,20], resulting in a large number of stress events per unit volume or time [21]. Milling and comminution of particles down to 1 μm may be suitably described by Kwade's stress model [22], which describes comminution in terms of i) the stress number, SN; and ii) the stress energy of the grinding media, SE_{GM} [23]:

$$SN = \frac{\varphi_{GM}(1-\epsilon)}{(1-\varphi_{GM}(1-\epsilon))c_v}\frac{n\,t}{d_{gm}} \quad (1)$$

$$SE_{GM} \propto {d_{GM}}^3 \cdot \rho_{GM} \cdot {v_t}^2 \quad (2)$$

where the stress number (SN) describes the average number of particle stress events in batch media milling, accounting for the grinding media fill ratio (φ_{GM}), diameter (d_{GM}) and porosity (ϵ); as well as the rotational speed of the stirrer (n), residence time (t) and the volume concentration of the suspension (c_v). The stress energy of the grinding media (SE_{GM}) is related to the grinding media diameter and density (ρ_{GM}), and the circumferential velocity of the stirrer tip (v_t).

Optimized milling parameters are often discussed in relation to Kwade's stress model. However, for ultra-fine grinding (<1 μm), particle–particle interactions should be considered, with the aggregate particle size corresponding to the balance between aggregation, deaggregation and comminution. This complexity is particularly true for TiO_2 pigment milling, which is wholly an agglomerate milling process, with the aim to break aggregates towards the primary particle size [24]. Moreover, poor colloidal stability may induce poor flowability of the suspension, influencing both the energy consumption of the mill and the stress mechanism prevalent within the mill [25].

Electrostatically-stabilised wet milling has been studied by Stenger et al. [22], with appropriate suspension control by pH moderation likely providing stabilization of α-aluminum oxide particles milled down to 10 nm (determined by acoustic spectroscopy). Although, stabilization of the nanoparticles may have been influenced by dissolution of alumina hydroxide. Peukert et al. [26] observed similarly small stable particles (10 nm) when milling tin oxide using a stirred media mill, with the particles electrostatically-stabilised at pH 11, when no mechanochemical changes were observed.

Milling of heterogeneous particles is limited to clay minerals in dry ball mills, where cleavage along the basal plane initially exposes new basal planes, before particle breakage perpendicular to the basal plane may also be observed [27]; with amorphisation reported after prolonged milling treatment [28]. Vdović et al. [29] showed an increase in the particle $pH_{i.e.p.}$ when separately milling ripidolite and kaolinite clay mineral particles, confirming the increased presence of amphoteric edge surfaces. To the authors' knowledge, there is little consideration of surface properties of Al-doped TiO_2 during milling, a discretely heterogeneous system, where the surface governs milling performance and additive activity.

The current study considers the changing surface properties (particle zeta potential and surface composition) of Al-doped TiO_2 as a function of the primary particle size during milling at a range of mill speeds from 2500 to 8000 rpm. The particle properties were characterized by particle size, particle zeta potential, BET, XPS and TEM.

2. Materials and experimental methods

Research grade Al-doped TiO_2 was supplied by Venator Pigments UK Ltd. The sample showed a bimodal particle size distribution and d_{50} of 1.23 μm (Fig. 1). The received slurry was washed using deionised water (5 L) and left to settle for 2 weeks before syphoning off the supernatant. The wash process was repeated 3 times. The sample (of mass ~3 kg) was dried at 100 °C in an oven for 24 h. All suspensions were prepared in 10^{-3} M NaCl background electrolyte (analytical grade, Sigma-Aldrich) using Milli-Q water.

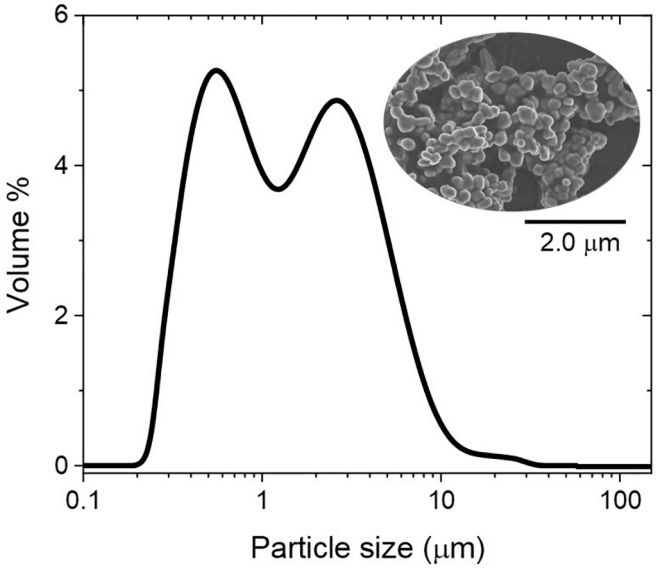

Fig. 1. Particle size distribution of the as-received Al-doped TiO_2. A suspension of 5 vol% was prepared in 10^{-3} M NaCl and adjusted to pH 4 to disperse the Al-doped TiO_2 particles. Inset: scanning electron microscope image of the dried Al-doped TiO_2 particles.

2.1. Stirred wet mill

A stainless steel grinding chamber (of volume 365 mL excluding spindle) and ceramic spindle (Supplementary Fig. S1) were fabricated for use with a Silverson high shear mixer (L5M-A, Silverson, UK). The mill was operated with a 0.8 grinding media fill ratio, using zirconia coated silica milling beads of 500 μm diameter. After each experiment the grinding media was washed in excess deionised water and sieved between 350 and 560 μm to remove any potential fragmented milling beads prior to reuse. Suspensions were prepared to 22 wt% Al-doped TiO_2 (~5 vol%) in 10^{-3} M NaCl and adjusted with 10^{-3} M HCl to pH 4. Suspensions were stirred for several hours using a magnetic stirrer bar to ensure the suspensions were well-mixed and at equilibrium prior to use. Suspensions of volume 75 mL were transferred to the grinding chamber and the spindle set to 100 rpm for 1 min to allow the suspension to coat the milling beads. The mill was then operated at the chosen stirrer speed and the suspension milled for different times.

For milledm samples characterized by X-ray diffraction (XRD), X-ray photoelectron spectroscopy (XPS) and BET, the mill was stopped at a predetermined time and the suspension was drained from the grinding chamber through a sieve. Milli-Q water was used to rinse the grinding chamber/media to ensure sufficient sample was collected for further analysis. For zeta potential and particle sizing measurements, a smaller sample volume was required, therefore the mill was temporarily stopped at the predetermined time and 150 μL aliquots of the suspension were pipetted into 15 mL Eppendorf tubes made up with 14.85 mL of 10^{-3} M NaCl at pH 4. To ensure the sample volume reduction did not influence the long-time mill behavior, a maximum of 5 samples were collected from a single milling test.

2.2. Zeta potential

The pH-dependent zeta potential of the particles was measured using a Zetasizer Nano ZS (Malvern Panalytical, UK), applying the Henry-Smoluchowski approximation [30]. Milled suspensions were diluted to 200 ppm (solids basis) in 10^{-3} M NaCl at pH 4. The suspension pH was then adjusted using 10^{-3} M HCl or 10^{-3} M NaOH before ultrasonication for 5 min and pipetting the sample into a Zeta Cell (DTS1070). All zeta potential measurements were conducted in triplicate, with the average values reported, and particle zeta potentials were measured over the pH range 3 to 11, with no fewer than 8 data points collected. Furthermore, several milled samples from different mill conditions were considered to determine the standard error associated with milling, with triplicate experiments and triplicate zeta potential measurements conducted. The standard error was then determined by $\Delta pH_{i.e.p.}/2$ (highest – lowest $pH_{i.e.p.}$).

2.3. Particle size

The particle size distribution (PSD) of particle clusters, referred to as the 'apparent' particle size, was measured using a Mastersizer 2000 (Malvern Panalytical, UK) with a hydro 2000 SM dispersion unit. Suspensions were collected from the mill and ultra-sonicated for 5 min. Samples were pipetted into the dispersion unit until the laser obscuration was within the optimum range of ~15 to 20% with a stirrer speed of 2200 rpm. Prior to pipetting the suspension, the dispersion unit and flow cell were filled with 10^{-3} M NaCl at pH 4 and no variation in pH was observed after adding the suspension. The particles were circulated through the measurement cell with the scattering intensity of the incident laser used to determine the PSD based on MIE theory [31].

2.4. Particle specific surface area

The 'true' particle size, referring to the primary particles, was determined from specific surface area analysis and estimated based on a sphere geometry. Brunauer, Emmett and Teller theory (BET) is an extension of the Langmuir theory, permitting application of such theory to multilayer adsorption, and was used to determine the particle surface area via nitrogen gas adsorption. Approximately 6 to 8 g of milled sample (solid mass) was heated at 100 °C in a vacuum oven overnight (<10 mmHg, ~12 h), before nitrogen adsorption was conducted using a Tristar 3000 (Micrometrics, USA). A 6 point adsorption method was used between the relative pressures $\left(\frac{\text{equilibrium pressure } (p_e)}{\text{saturation pressure } (p_o)}\right)$ of 0.04 and 0.1, where Langmuir-like monolayer adsorption is observed [32]. Results are plotted in the linear format of the BET equation to determine the specific surface area (Eq. (3)):

$$\frac{1}{v\left[\left(p/p\right)-1\right]} = \frac{c-1}{v_m c}\left(\frac{p}{p_0}\right) + \frac{1}{v_m c} \tag{3}$$

where v and v_m are the adsorbed gas volume and monolayer adsorbed gas volume respectively, and c the BET constant. Relation of v_m to the specific surface area is possible using the molecular area of the adsorbate, σ, and Avagadro's constant, N_a (Eq. (4)) [33].

$$SSA = \frac{v_m}{22414}\,\sigma N_a \tag{4}$$

The primary particle size (d_{prim}, nm), assuming non-aggregated spherical particles, is calculated (Eq. (5)) from the specific surface area (SSA) and particle density (ρ) which is taken to be 4.23 g cm^{-3}.

$$d_{prim} = {}^{6000}\!/_{SSA.\rho} \tag{5}$$

2.5. X-ray diffraction (XRD)

Dried powder (~5 g, 100 °C, 12 h) was gently ground using a pestle and mortar before being pressed into the sample holder. XRD spectra were collected using a Phillips X'pert 8 (Malvern Panalytical, UK) with a monochromatic CuKα radiation source (λ = 0.154 nm) over the 2θ range of 20 to 80°.

2.6. X-ray photoelectron spectroscopy (XPS)

XPS spectra of milled samples at stirrer speeds from 2500 to 6000 rpm were measured using a Kratos Axis-Supra XPS with a monochromatic Mg Kα X-ray source (1253.6 eV) operated at 225 W. For samples milled at 8000 rpm, a Therma NEXSA system was used, operating with a monochromatic Al Kα X-ray source (1486.69 eV) at 19 W. All samples were maintained under vacuum of $<10^{-9}$ Torr and survey scans were conducted with a pass energy of 160 eV. Samples were analysed in CasaXPS with Shirley backgrounds subtracted.

3. Results and discussion

3.1. Milling of Al-doped TiO_2

Fig. 2 shows the PSD of the non-milled and milled samples at a stirrer speed of 6000 rpm with milling times up to 60 min. The non-milled sample PSD is bimodal and likely results from agglomeration of submicron particles (SEM inset Fig. 1) induced by high temperatures in the flame synthesis of TiO_2 [5]. Within the first 2 min of milling, the bimodal PSD significantly reduces and a monamodal PSD was observed after 30 min. The initial decrease in PSD can be attributed to de-agglomeration of weakly interacting particle clusters, with the d_{50} decreasing by ~0.8 μm and the primary particle size decreasing by ~40 nm. With further milling, a monomodal particle size distribution results from both de-agglomeration and particle breakage, and at 60 min the d_{50} is 0.279 μm with a PSD ($d_{90} - d_{10}$) of 0.3 μm, from an initial condition of d_{50} = 1.25 μm and PSD = 4.2 μm.

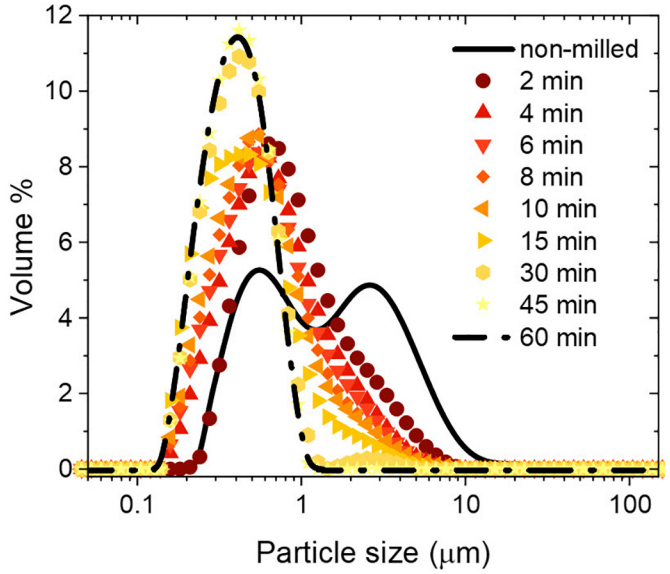

Fig. 2. Milling time-dependent particle size distribution for non-milled and milled samples at time intervals up to 60 min at 6000 rpm stirrer speed. Suspension properties: 5 vol% Al-doped TiO_2 and pH = 4.

3.2. Stirrer speed milling performance

Fig. 3a and b show mill curves for 5 vol% Al-doped TiO_2 at four different stirrer speeds of 2500, 4000, 6000 and 8000 rpm. The particle d_{50} and PSD (d_{90} – d_{10}) for the grey-shaded symbols (2500, 4000 and 6000 rpm) represent behavior as described by Kwade's analytical stress model [23]. The model describes increased milling kinetics for increased stirrer speeds, with behavior attributed to the increase in stress number and stress energy. At 8000 rpm (blue symbols), Fig. 3a and b show a decrease in the initial milling kinetics (0–10 min), even though a similar d_{50} ~0.3 μm is attained after 60 min milling. The milling kinetics are compared (Supplementary Fig. S2) as a function of the first-order rate equation [34] (Eq. (6), where d_{50} is the median particle size at time t), with the milling kinetics suitably described by three first order rate constants, k_1, k_2 and k_3 (Table 1 and Supplementary Table S1); which describe de-agglomeration of weakly interacting agglomerates (formed during the high temperature particle flame synthesis) [5] (0–2 min); de-aggregation of strong particle clusters (2–10 min); and the slow kinetics during the final 45 min of milling (15–60 min), where particle size reduction is dependent on the shift in equilibrium between de-aggregation and aggregation.

Table 1
Breakage rate constant k_1 (0 – 2 min) and respective R^2 values as a function of stirrer speed. Breakage rate constants are compared in Table S1 of the Supplementary Information.

Stirrer speed (rpm)	Breakage constant k_1
2500	0.221
4000	0.351
6000	0.379
8000	0.330

At 8000 rpm, k_1 is between the rate constants for 2500 and 6000 rpm stirrer speeds, confirming a change in the initial milling phenomena and deviation from Kwade's analytical stress model [23]. k_1 only describes the first 2 min of milling, but its influence is significant, with the particle size (d_{50} and PSD) at 8000 rpm being larger than 6000 rpm for milling times between 2 and 45 min.

$$-\frac{dd_{50}}{dt} = k_i d_{50t} \tag{6}$$

Beyond the stress energy, the 3-fold increase in stirrer speed (2500 to 8000 rpm) can change the flow field within the mill, altering the relationship between impact and shear related breakage. Eskin et al. [35] described two milling regimes: i) uniform dispersion of milling beads when turbulent dispersion forces exceed centrifugal forces; and ii) radial stratification when centrifugal forces exceed turbulent dispersion forces. It is feasible that the change in initial milling performance at 8000 rpm relates to a change in the flow regime, with shear dominated breakage plausible at higher stirrer speeds.

For ultra-fine milling, Knieke et al. [36] described the *apparent* and *true* grinding limits which relate to the plateau in aggregate size and particle size, respectively. For polycrystalline materials, the particle size may be suitably described by the primary particle size, assuming breakage occurs at grain boundaries. It is perceived that below a critical particle size, the stress energy of media bead–bead collision is insufficient for brittle fracture and breakage occurs via lattice imperfections due to the build-up of elastically stored energy [36]. For example, Biligilli et al. [37] reported non-linear first order breakage, with milling behavior transitioning from de-agglomeration to *true* particle breakage at extended milling times, considered to be a consequence of particle fatigue. The *apparent* grinding limit depends on the interparticle interactions and suspension stability, and in the current study, particles were electrostatically stable at pH 4, with the apparent grinding limit independent of stirrer speed, as seen by a plateau in the apparent particle size (d_{50} ~0.3 μm) after 60 min milling. When considering the *true* particle breakage limit, a plateau in the primary particle size is almost observed for stirrer speeds of 2500 and 4000 rpm, but not at higher

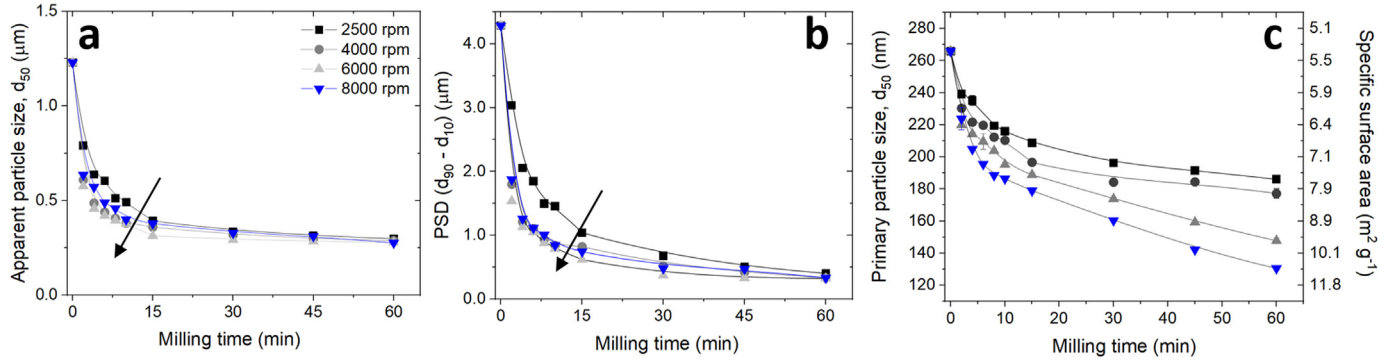

Fig. 3. Milling performance (a) d_{50}, (b) PSD (d_{90} – d_{10}), and (c) primary particle size (determined from the SSA which is shown as an inverse-scale on the Y2-axis) as a function of milling time and stirrer speed. Suspensions of 5 vol% Al-doped TiO_2 were prepared in 10^{-3} M NaCl at pH 4. Arrows indicate the theoretical improvement in milling performance with increased stirrer speed as described by Kwade's analytical stress model. A clear deviation from the analytical stress model behavior is observed at 8000 rpm stirrer speed.

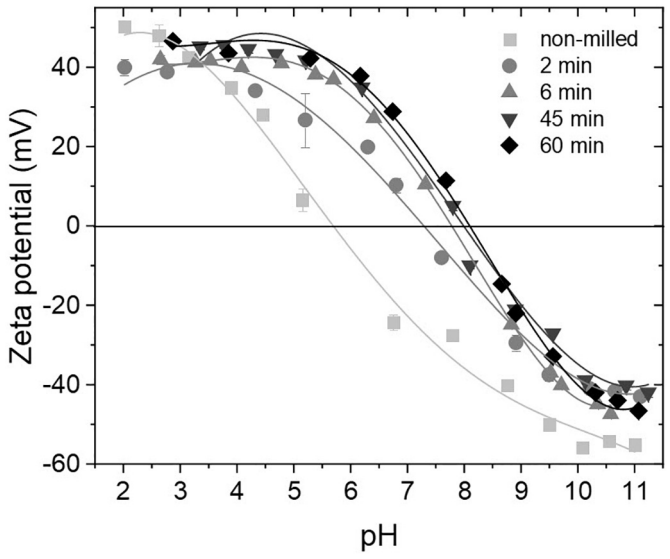

Fig. 4. Milling time-dependent zeta potential curves of Al-doped TiO_2 milled at 5 vol% in 10^{-3} M NaCl at pH 4 and 6000 rpm.

stirrer speeds, where the primary particle size continues to decrease (Fig. 3c).

3.3. Surface chemistry of Al-doped TiO_2

The $pH_{i.e.p.}$ of the non-milled sample was pH 5.7, in good agreement with rutile TiO_2, $pH_{i.e.p.}$ ~6 [38], and within the reported $pH_{i.e.p.}$ range of 4 to 6, with variation attributed to the synthesis procedure, polymorph and crystal facet studied [39]. Fig. 4 shows the zeta potential curves for Al-doped TiO_2 milled at 6000 rpm for 2, 6, 45 and 60 min. The $pH_{i.e.p.}$ shifts to more basic pH with increased milling time, reaching a steady state $pH_{i.e.p.} = 8.1$ at around 45 min. With increased milling time the $pH_{i.e.p.}$ shifts closer to that of α-aluminum oxide ($pH_{i.e.p.}$ ~9) [38], suggesting a change in the type and concentration of hydroxyl sites on the particle surface. Similar changes in the electrochemistry of Al-doped TiO_2 have been reported by Taylor et al. [9], studying the effect of Al_2O_3 dopant concentration on the synthesis of Al-doped TiO_2 by the chloride process. Taylor et al. [9] reported a $pH_{i.e.p.} = 9.1$ with a dopant concentration of 1.2 wt% (Al_2O_3). In the current study, particles were synthesized via the chloride process and doped with ~1 wt% $AlCl_3$.

The $pH_{i.e.p.}$ of Al-doped TiO_2 is compared as a function of milling time and stirrer speed, see Fig. 5a. For all stirrer speeds and with extended milling times (30–60 min), the $pH_{i.e.p.}$ values reach steady state, which for milling speeds of 2500, 4000 and 6000 rpm is in the range of $pH_{i.e.p}$ ~7.9 to 8.1, and at 8000 rpm is lower at $pH_{i.e.p.}$ ~6.7. At short milling times (<6 min) and independent of the stirrer speed, the standard measurement error was ±0.5 pH units, which reduced to ±0.2 pH units at longer milling times. High variability at short milling times is attributed to the large variation in stress intensities and stress numbers, with greater uniformity achieved by extended milling. The wider sample variation at short milling times is also reflected by the larger PSD ($d_{90} - d_{10}$) of Al-doped TiO_2 – 6000 rpm: PSD @ 6 min = 1.05 μm; PSD @ 60 min = 0.33 μm.

To understand the apparent changes in surface chemistry of Al-doped TiO_2, the $pH_{i.e.p.}$ was compared to the particle SSA (determined by nitrogen adsorption) of milled Al-doped TiO_2 (Fig. 5b). The grey symbols (stirrer speeds of 2500, 4000 and 6000 rpm) superimpose onto a single master curve (solid line), and confirm the correlation between particle surface chemistry and particle SSA. The steady-state values of $pH_{i.e.p.}$ 7.8 to 8.1 correspond to particle SSA values of 7.62 to 9.6 m^2/g (slight dependence on stirrer speed), with SSA > 8 m^2/g measured at 6000 rpm but with no measurable increase in the $pH_{i.e.p.}$, which may reflect similarity between the particle bulk and particle surface properties. At 8000 rpm, the particle SSA of the milled Al-doped TiO_2 sample increases to 11 m^2/g, although the change in $pH_{i.e.p.}$ is negligible when SSA > 7.5 m^2/g, similar to samples milled at lower stirrer speeds. While comparable SSA values (6–8 m^2/g) were measured, the 8000 rpm sample does not fit the single master curve, and likely supports our previous discussion around a different particle breakage mechanism during milling.

The difference in $pH_{i.e.p.}$ with stirrer speed may result from mechanochemical changes. Dissolution of alumina hydroxide from α-aluminum oxide has been reported when 5 > pH > 9 [40] and shown to alter the particle zeta potential [41]. Stenger et al. [22] studied wet milling of α-aluminum oxide over extended mill times (t ≥120 min) and confirmed the formation of bayerite and in some cases bayerite and gibbsite. The estimated layer thickness of precipitated hydroxide was comparable when studied by differential scanning calorimetry (DSC), thermogravimetric analysis (TGA) and XRD. In the current study, XRD analysis of Al-doped TiO_2 milled at different stirrer speeds for 60 min confirmed no mechanochemical changes, with all XRD peaks identifiable as rutile TiO_2 (Supplementary Fig. S3). Moreover, Stenger et al. [22] observed an endothermic peak at ~280 °C which was attributed to the transformation of bayerite to Al_2O_3 ($2Al(OH)_3 \rightarrow Al_2O_3 + 3H_2O$), and from TGA analysis, a mass loss (defined as $\frac{\Delta m}{m}$, where m is the

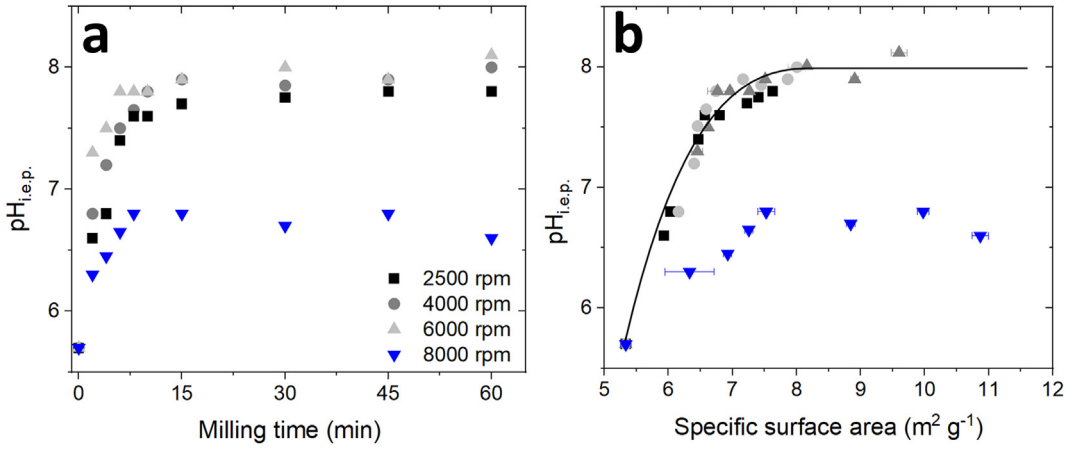

Fig. 5. a) $pH_{i.e.p.}$ of Al-doped TiO_2 as a function of the milling time, b) BET SSA of milled Al-doped TiO_2 at stirrer speeds of 2500 to 8000 rpm (symbols shown in Fig. 5a). Solid line is added to guide the eye.

sample mass) of 13% was measured over the temperature range 250 to 900 °C, which was attributed to the concurrent formation of water and Al_2O_3, and subsequent evaporation of water. In the current study, TGA and DSC were used to analyse samples milled at 6000 and 8000 rpm for 60 min (Supplementary Fig. S4a and b), and with no characteristic transitions observed, it can be concluded that the differences in $pH_{i.e.p.}$ do not result from mechanochemical changes.

The atomic concentrations (at.%) of O, Ti and Al were determined from XPS analysis (Fig. 6C) of the non-milled and 9 milled samples of Al-doped TiO_2 at all stirrer speeds, collected at mill times >6 min. The particle surface Al content (at.%) as a function of particle SSA (and ΔSSA) and particle $pH_{i.e.p.}$ is shown in Fig. 6, along with the XPS spectra showing all major elemental peaks. These peaks include the O_{1s}, Ti_{2p} and Al_{2p} electron orbitals used to determine the relative surface content of alumina. Other peaks include adventitiously adsorbed carbon (C_{1s}), nominal chlorine (Cl_{2p}), which is likely adsorbed during the chloride process (as noted by Taylor et al. [9]) and silica (Si_{2p}), expected to be a contaminant from the grinding media.

For all samples, thet particle surface Al content (at.%) shows an approximate linear correlation ($R^2 = 0.87$) to the particle SSA (Fig. 6a), indicating through the cleavage of bonds, new surface alumina sites (hydroxyl sites) are exposed (to note, the alumina hydroxyl sites are surface hydroxyl groups spontaneously formed when alumina is dispersed in water, as opposed to the stable polymorphic forms probed using DSC/TGA – namely, bayerite and gibbsite, as previously discussed). The correlation holds for all stirrer speeds, however when compared against $pH_{i.e.p.}$ (Fig. 6b), only the milled samples at stirrer speeds between 2500 and 6000 show a gradual increase in $pH_{i.e.p.}$ with increasing Al content (this trend omits the non-milled sample where Al content (at.%) is relatively low, ~4 at.%, and the concentration reported may be biased by sub-surface Al).

With a penetration depth of 4 nm (~20 monolayers) for Al-doped TiO_2 [9,42], XPS is not perfectly surface sensitive, thus correlating Al content (at.%) to the particle $pH_{i.e.p.}$ may lead to slight variation between the two data sets. Moreover, $pH_{i.e.p.}$ is a surface area weighted average, whereas XPS is localized, hence further discrepancy between the two measurement techniques is reasonable. Consequently, the R^2 value is deemed suitable to confirm an approximate linear correlation between $pH_{i.e.p.}$ and Al content (at.%). Hence, for stirrer speeds between 2500 and 6000 rpm, the shift in $pH_{i.e.p.}$ can be attributed to the increased particle surface heterogeneity (increasing Al content). Studying TiO_2 samples (synthesized via the chloride process) with dopant (Al_2O_3) concentrations ranging from 0.33 to 1.18 wt%, Taylor et al. [9] showed a similar linear correlation between $pH_{i.e.p.}$ and Al content (at.%), albeit the Al content (at.%) required to achieve similar $pH_{i.e.p.}$ values was generally lower than those reported in the current study; for example, 4.6 at.% Al for $pH_{i.e.p.} = 8.2$, compared to ~9.5 at.% Al for $pH_{i.e.p.} = 8.0$ in the current study.

A discrepancy between 8000 rpm and the slower stirrer speeds was found when plotting Al content (at.%) vs. $pH_{i.e.p.}$ but not for Al content (at.%) vs. SSA. While equivalent Al contents (at.%) were observed for all milled samples, the $pH_{i.e.p.}$ for 8000 rpm was lower than those measured at slower stirrer speeds. Further examination of the pH-dependent zeta potential curves (Supplementary Fig. S5) also reveal a slight reduction in the magnitude of the maximum zeta potentials (at $pH < 4$ and $pH > 10$), with values not exceeding ±40 mV. Kanta et al. [39] and Yang et al. [43] report such behavior (reduced magnitude of zeta potentials) to result from temperature (≥500 °C) induced dehydroxylation of both amorphous TiO_2 and α-aluminum surfaces. An attempt to confirm if surface dehydroxylation occurs at 8000 rpm and not 6000 rpm was made using dynamic vapor sorption (DVS); considering two samples of similar surface areas (7.52 and 7.26 m^2/g for 8000 and 6000 rpm, respectively). DVS is a useful technique to probe surface hydroxyl groups with water adsorption being significantly affected by the concentration of surface oxygen moieties (the ability to hydrogen bond). The DVS isotherms (Supplementary Fig. S6) for both samples showed negligible hysteresis with the maximum adsorbed amount of H_2O, normalized by the sample SSA (determined from gaseous nitrogen adsorption), found to be 12.3% lower for the 8000 rpm sample (see Supplementary Table S2 for full analysis). While the normalized mass of H_2O adsorbed is slightly lower than the 6000 rpm sample, hinting at surface dehydroxylation, variation between the two samples can be considered insignificant and thus surface dehydroxylation cannot conclusively account for such differences in $pH_{i.e.p.}$.

The 'apparent' milling performance (Fig. 3a and b) follows Kwade's analytical stress model up to 6000 rpm, with deviation from the model and poorer milling performance observed at 8000 rpm. However, when considering the 'true' breakage behavior, enhanced milling performance can be observed for each increase in stirrer speed (2500 to 8000 rpm). Using TEM images to conduct a particle size analysis (Supplementary Fig. S8), little variation in particle size and distribution was observed (minimum discernible size = 50 nm). However, the TEM images of Al-doped TiO_2 milled at 8000 rpm for 60 min (Fig. 7) revealed the presence of many spherical ultra-fines (≪50 nm) which surface coated the coarser particles (d_{50} ~ 0.3 μm). The higher SSA values at 8000 rpm (Fig. 3C) can be attributed to the significant presence of these ultra-fines, which were not observed at 2500 rpm (Fig. 7). Analogous ultra-fines have also been reported by Elliot et al. [24] who considered

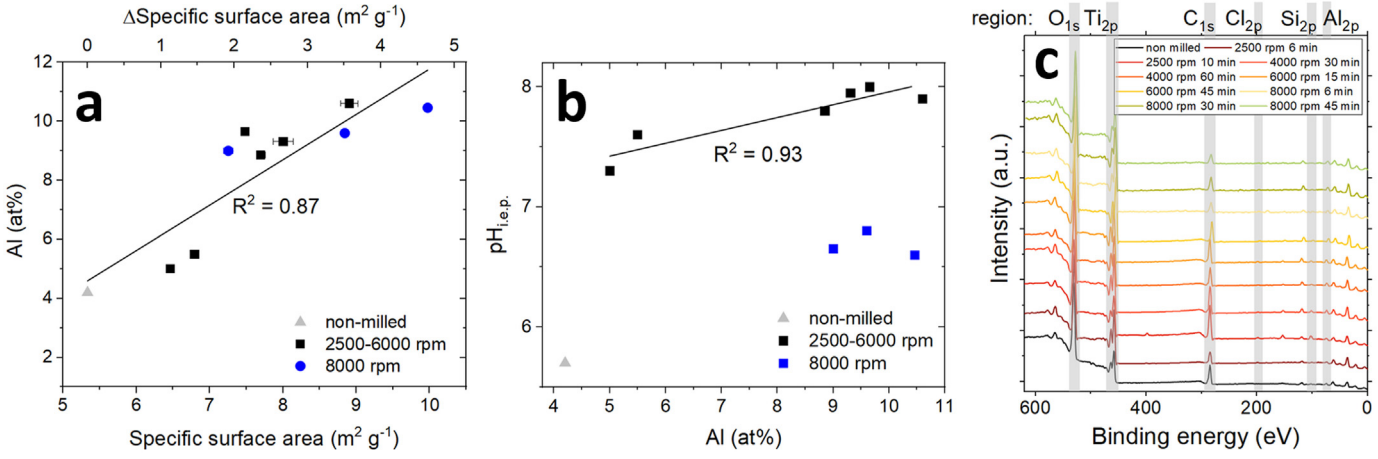

Fig. 6. The changing particle surface Al content (at.%) during milling of Al-doped TiO_2 as a function of the (a) particle SSA and (b) particle $pH_{i.e.p.}$. ΔSSA is calculated relative to the non-milled sample (ΔSSA = 0). (c) XPS spectra used to determine the relative content of surface alumina. XPS spectra for different mill times and stirrer speeds are shown in the figure legend. Highlighted regions represent the O_{1s}, Ti_{2p}, C_{1s}, Cl_{2p}, Si_{2p} and Al_{2p} peaks.

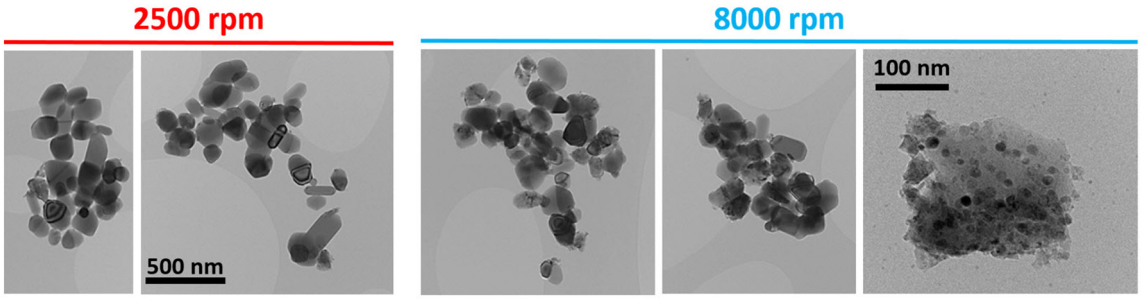

Fig. 7. TEM images of Al-doped TiO_2 milled for 60 min at 2500 and 8000 rpm. Scale bar of 500 nm is relevant for those images without a scale bar.

the stirred wet milling of Al-doped TiO_2 at 12000 rpm. Based on this finding, it can be hypothesized that these ultra-fines are formed by surface erosion of individual primary particles, as suggested by Gesenhues [44], a consequence of the high shear milling behavior. With the ultra-fines exhibiting more titania-like surface properties (non-milled sample, $pH_{i.e.p.} = 5.7$), they are able to screen the 'true' surface potential of the larger primary particles which leads to the apparent discrepancy in $pH_{i.e.p.}$ between 8000 rpm and the slower stirrer speeds (Fig. 5). Explicitly, the reduction in breakage rate constant at 8000 rpm compared to 6000 rpm is unlikely to account for the generation of ultra-fines, since the particle size is below the detection limit of the light scattering technique. As such, the 'apparent' milling performance at 8000 rpm is likely to be enhanced, although the effect is difficult to quantify. However, from this study and observed by others [24,44], milling at 8000 rpm (very high shear) certainly induces a change in the milling behavior, with the Al-doped TiO_2 particles undergoing both fracture and surface erosion induced breakage, with the latter resulting in the observed ultra-fines.

4. Conclusions

The relationships between stirred wet milling performance, particle breakage mechanism, and the surface chemistry of Al-doped TiO_2 has been studied. An increase in the 'apparent' aggregate breakage was observed when increasing the stirrer speed from 2500 to 6000 rpm, with the initial milling performance reduced at 8000 rpm. However, considering the 'true' particle breakage, milling performance improved for each incremental increase in stirrer speed. Analysis of TEM images revealed that the enhanced 'true' particle breakage at 8000 rpm resulted from the generation of many ultra-fines ($d_{50} \ll 50$ nm) which were not observed at slower stirrer speeds. These ultra-fines were found to coat the larger primary particles which accounted for the slightly lower $pH_{i.e.p.}$ of the 8000 rpm sample compared to samples milled at all other stirrer speeds.

The particle surface Al content (at.%) increased approximately linearly with particle SSA, and the changing $pH_{i.e.p}$ for all samples was attributed to increased exposure of surface alumina hydroxyls. Good agreement between particle surface Al content (at.%) and particle SSA was found for all samples. However, when compared against the particle $pH_{i.e.p.}$, the 8000 rpm data did not follow the trend observed at slower stirrer speeds. The discrepancy was attributed to the generation of ultra-fines which screened the 'true' particle zeta potential. The smaller shift in $pH_{i.e.p.}$ when milled at 8000 rpm suggested that the ultra-fines were predominantly titania-like and suppressed the shift in $pH_{i.e.p.}$ as the particle surface Al content (at.%) increased. At extended milling times, all samples reached a constant value of $pH_{i.e.p.}$ when the particle surface properties reflected the particle bulk properties. For the Al-doped TiO_2 sample, the bulk particle is enriched in Al.

The study highlights the importance of characterizing surface properties when milling heterogeneous particles into the colloidal-size range. With decreasing particle size, the influence of the changing surface properties can become magnified, potentially altering the interaction between the particles and particle-dispersant molecules, thus directly impacting the suspension viscosity and milling performance. At pH 4, and independent of the evolving surface chemistry, the particles remained highly charged, thus the effect observed in the current study was negligible. However, when milled at pH 9 (data not considered in the current study), significant thickening of the suspension was observed as the $pH_{i.e.p.}$ shifts to more basic pHs. Under such conditions particle aggregation is strong, leading to increased viscous dampening of the media bead motion and reduced milling performance.

Data statement

Austin, D., Hassanpour, A., Hunter, T.N., Robb, J., Edwards, J.L., Sutcliffe, S., Lee, J.W., Harbottle, D., (2020): Data associated with 'Evolving Surface Properties of Stirred Wet Milled Aluminum-Doped Titanium Dioxide: A Discretely Heterogeneous System', University of Leeds. [Dataset]. https://doi.org/10.5518/883. Article metadata is available under a Creative Commons Attribution licence (CC-BY) [45].

Declaration of Competing Interest

The authors declare that they have no known competing financial interests or personal relationships that could have appeared to influence the work reported in this paper.

Acknowledgements

This research was completed at the EPSRC Centre for Doctoral Training in Complex Particulate Products and Processes (EP/L015285/1), in collaboration with Venator Ltd., who we gratefully acknowledge for their support of this work. The authors would like to acknowledge the Harwell XPS facilities for analysis of the 8000 rpm milled samples, which was performed at the EPSRC National Facility for XPS ('HarwellXPS'), operated by Cardiff University and UCL, under contract No. PR16195. The authors thank Dr. Beth Willneff of the Versatile X-ray Spectroscopy Facility (VXSF) at the University of Leeds, where XPS user training and preliminary data collection was conducted. Dr. Ben Douglas, Adrian Cunliffe and Karine Alves Thorne at the University of Leeds are acknowledged for analytical support.

Appendix A. Supplementary data

Supplementary data to this article can be found online at https://doi.org/10.1016/j.powtec.2020.09.033.

References

[1] J.H. Braun, A. Baidins, R.E. Marganski, Prog. Org. Coat. 20 (1992) 105–138.
[2] F. Karakaş, M.S. Çelik, Colloids Surf. A Physicochem. Eng. Asp. 434 (2013) 185–193.
[3] K. Ohenoja, M. Illikainen, J. Niinimäki, Powder Technol. 234 (2013) 91–96.

[4] M.M. Islam, T. Bredow, A. Gerson, Phys. Rev. B Condens. Matter. Mater. Phys. 76 (2007) 045217.
[5] H. Bel Fadhel, C. Frances, A. Mamourian, Powder Technol. 105 (1999) 362–373.
[6] V. Juergens, S. Bleumel, A. Abdin, J. Friedrich, V. Schmitt, Production of Titanium Dioxide Pigment Obtainable by the Sulfate Process with a Narrow Particle Size Distribution, 2017 Pub. No.: US 2017/0210906 A1, United States Patent Application Publication.
[7] S. Farrokhpay, Adv. Colloid Interf. Sci. 151 (2009) 24–32.
[8] M.K. Akhtar, Y. Xiong, S.E. Pratsinis, AICHE J. 37 (1991) 1561–1570.
[9] M.L. Taylor, G.E. Morris, R.S.C. Smart, J. Colloid Interface Sci. 262 (2003) 81–88.
[10] S. Vemury, S.E. Pratsinis, J. Am. Ceram. Soc. 78 (1995) 2984–2992.
[11] C.Y. Tsai, T.H. Kuo, H.C. Hsi, Int. J. Photoenergy (2012) https://doi.org/10.1155/2012/874509.
[12] M.K. Akhtar, S.E. Pratsinis, S.V.R. Mastrangelo, J. Mater. Res. 9 (1994) 1241–1249.
[13] R. Shirley, M. Kraft, O.R. Inderwildi, Phys. Rev. B Condens. Matter. Mater. Phys. 81 (2010) 1–9.
[14] M. Steveson, T. Bredow, A.R. Gerson, Phys. Chem. Chem. Phys. 4 (2002) 358–365.
[15] R.A. Slepetys, P.A. Vaughan, J. Phys. Chem. 73 (1969) 2157–2162.
[16] F. Garbassi, E. Melloceresa, E. Occhiello, L. Pozzi, M. Visca, D.M. Lenti, Langmuir 3 (1987) 173–179.
[17] U. Gesenhues, Solid State Ionics 101–103 (2002) 1171–1180.
[18] L.-S. Johansson, T. Losoi, Surf. Interface Anal. 17 (1991) 230–236.
[19] A. Kwade, Powder Technol. 105 (1999) 14–20.
[20] R. Hogg, H. Cho, KONA Powder Part. J. 18 (2000) 9–19.
[21] A. Kwade, J. Schwedes, KONA Powder Part. 15 (1997) 91–102.
[22] F. Stenger, S. Mende, J. Schwedes, W. Peukert, Powder Technol. 156 (2005) 103–110.
[23] A. Kwade, Chem. Eng. Technol. 26 (2003) 199–205.
[24] L.N. Elliott, J.S. Behra, N. Hondow, R.A. Bourne, A. Hassanpour, J.L. Edwards, S. Sutcliffe, T.N. Hunter, J. Colloid Interface Sci. 548 (2019) 110–122.
[25] M. Sommer, W. Peukert, *Handbook of* Powder Technology, 12, 2007 551–603.
[26] F. Stenger, S. Mende, J. Schwedes, W. Peukert, Chem. Eng. Sci. 60 (2005) 4557–4565.
[27] I. Sondi, M. Stubičar, V. Pravdić, Colloids Surf. A Physicochem. Eng. Asp. 127 (1997) 141–149.
[28] É. Makó, R.L. Frost, J. Kristóf, E. Horváth, J. Colloid Interface Sci. 244 (2001) 359–364.
[29] N. Vdovic, I. Jurina, S.D. Škapin, I. Sondi, Appl. Clay Sci. 127 (2010) 575–580.
[30] J. Gregory, Particles in Water: Properties and Processes, Taylor & Francis, 2006.
[31] Malvern Instrument limited, *Malvern Mastersizer 2000 User Manual*, MAN0384 edn. 2007.
[32] K.Y. Foo, B.H. Hameed, Chem. Eng. J. 156 (2010) 2–10.
[33] S.R. Chauruka, A. Hassanpour, R. Brydson, K.J. Roberts, M. Ghadiri, H. Stitt, Chem. Eng. Sci. 134 (2015) 774–783.
[34] K. Barani, H. Balochi, Physicochem. Probl. Miner. Process. 52 (2016) 268–278.
[35] D. Eskin, O. Zhupanska, R. Hamey, B. Moudgil, B. Scarlett, AICHE J. 51 (2005) 1346–1358.
[36] C. Knieke, M. Sommer, W. Peukert, Powder Technol. 195 (2009) 25–30.
[37] E. Bilgili, R. Hamey, B. Scarlett, Chem. Eng. Sci. 61 (2006) 149–157.
[38] M. Kosmulski, Adv. Colloid Interf. Sci. 152 (2009) 14–25.
[39] A. Kanta, R. Sedev, J. Ralston, Langmuir 21 (2005) 2400–2407.
[40] C.F. Baes, R.S. Mesmer, The Hydrolysis of Cations, John Wiley & Sons, New York, 1976.
[41] J. Lützenkirchen, A. Abdelmonem, R. Weerasooriya, F. Heberling, V. Metz, R. Marsac, Geochem. Trans. 15 (2014) 1–14.
[42] G.E. Morris, W.A. Skinner, P.G. Self, R.S.C. Smart, Colloids Surf. A Physicochem. Eng. Asp. 155 (1999) 27–41.
[43] D. Yang, M. Krasowska, R. Sedev, J. Ralston, Phys. Chem. Chem. Phys. 12 (2010) 13724.
[44] U. Gesenhues, J. Nanopart. Res. 1 (1999) 223–234.
[45] D. Austin, A. Hassanpour, T.N. Hunter, J. Robb, J.L. Edwards, S. Sutcliffe, J.W. Lee, D. Harbottle, University of Leeds, 2020. https://doi.org/10.5518/883.